Production mechanism of doubly charmed exotic mesons T_{cc}

Hee-Jin Kim[1] and Hyun-Chul Kim[1,2,3]

[1]*Department of Physics, Inha University, Incheon 22212, Republic of Korea*
[2]*Physics Research Institute, Inha University, Incheon 22212, Republic of Korea*
[3]*School of Physics, Korea Institute for Advanced Study (KIAS), Seoul 02455, Republic of Korea*

(Received 16 July 2025; accepted 27 October 2025; published 14 November 2025)

We investigate the production mechanism for doubly charmed tetraquark mesons within a coupled-channel formalism. The two-body Feynman kernel amplitudes are constructed using effective Lagrangians that respect heavy quark symmetry, chiral symmetry, SU(3) flavor symmetry, and hidden local symmetry. The fully off-shell coupled scattering equations are solved within the Blankenbecler-Sugar reduction scheme. We find three positive-parity and one negative-parity tetraquark states with total spin $J = 1$. Among them, two positive-parity states appear as bound states in the isoscalar and isovector DD^* channels, while another appears as a resonance in the D^*D^* channel. A negative-parity resonance is also predicted in the isoscalar channel. We analyze the coupling strengths of these tetraquark states to various channels. The dependence of the results on the reduced cutoff mass Λ_0 is examined. The most significant tetraquark state remains stable within the range of $\Lambda_0 = (600\text{–}700)$ MeV.

DOI: 10.1103/5v1l-bqfw

I. INTRODUCTION

Since the Belle Collaboration announced the existence of the $X(3872)$, which is also known as $\chi_{c1}(3872)$ [1], the understanding of hidden-charm tetraquark states has undergone remarkable development both experimentally and theoretically (see the following reviews and references therein [2–7]). In 2022, the LHCb Collaboration reported the discovery of the first doubly charmed tetraquark state, $T_{cc}(3875)^+$, observed as a narrow enhancement near the D^0D^{*+} mass threshold [8]. Its Breit-Wigner mass was found to lie just below the D^0D^{*+} threshold with a remarkably narrow width of (410 ± 164) keV. The quantum numbers are tentatively assigned as $I(J^P) = 0(1^+)$, though an isovector assignment has not been definitively excluded by current data. Notably, approximately 90% of the observed $D^0D^0\pi^+$ events in the energy region between the D^0D^{*+} threshold and 3.9 GeV contain a genuine D^{*+} meson [9]. This recent finding of the $T_{cc}(3875)^+$ tetraquark state has triggered a great deal of theoretical work (see recent reviews and references therein [6,7]). Even before the observation of the $T_{cc}(3875)^+$, the existence of doubly charmed tetraquark states had already been speculated and investigated [10–23]. Theoretical studies can largely be divided into two categories: one considers the T_{cc} as a compact tetraquark state composed of four quarks [23–29], while the other views it as a molecular state of two D (D^*) mesons [7,30–49]. Lattice QCD studies [46,50,51] have demonstrated the presence of a pole in DD^* scattering near the physical point and have explored the isovector channel, suggesting possible additional exotic states in the doubly charmed sector.

Coupled-channel formalisms provide a very useful framework to analyze the production mechanisms of hadron resonances, particularly exotic ones (see, for example, recent reviews [52,53]). The dynamical generation of the $T_{cc}(3875)^+$ was also well described within several coupled-channel approaches [31–33,42,44]. Among the various coupled-channel approaches, we employ a formalism based on two-body Feynman kernel amplitudes, developed by the Bonn-Jülich group [54,55]. This approach has been successfully applied to a wide range of hadronic reactions, including $\pi\pi$ [56], $\pi\rho$ [57], $\pi\eta$ [58], πN [59], NN [60,61], and hyperon-nucleon [55,62] interactions. Whereas the Bonn-Jülich group employed time-ordered perturbation theory, we implement the Blankenbecler-Sugar (BbS) scheme [63,64], which is manifestly Lorentz covariant. We also adopt a more constrained treatment of the cutoff masses in the hadronic form factors to reduce uncertainties.

This coupled-channel formalism was successfully applied to the $\pi\rho$, $\pi\omega$, and $K\bar{K}^*$ coupled interactions [65–67], where the production mechanisms and internal structures of axial-vector mesons were explained: the a_1 meson can be interpreted as a $K\bar{K}^*$ molecular state [65], and b_1 mesons exhibit two-pole structures [66].

Published by the American Physical Society under the terms of the Creative Commons Attribution 4.0 International license. Further distribution of this work must maintain attribution to the author(s) and the published article's title, journal citation, and DOI. Funded by SCOAP³.

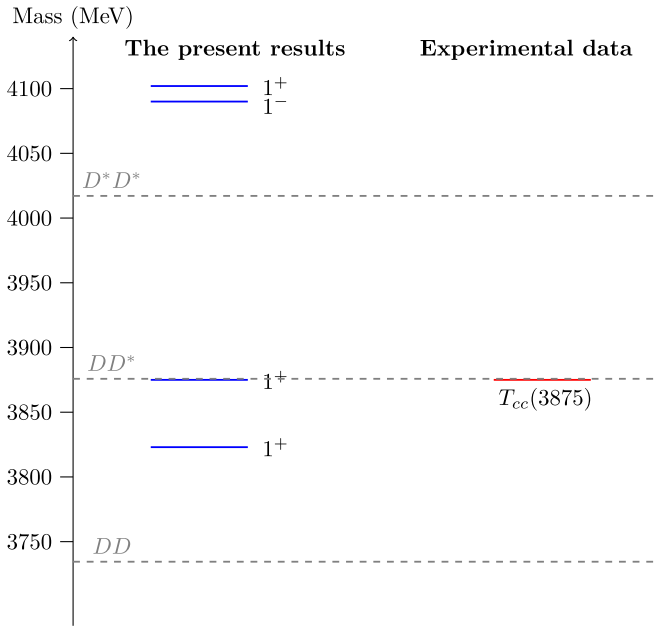


FIG. 1. Mass spectrum of T_{cc} states in the present work. The spin-parity quantum numbers are written for each state. The red line denotes the observed $T_{cc}(3875)$ by the LHCb Collaboration.

Furthermore, this approach clarified the discrepancies among existing experimental data for the h_1 mesons [67]. The framework was extended to the heavy-light sector, successfully describing the $D_{s0}^*(2317)$ as a DK molecular state [68]. It was also applied to explain how the hidden-charm pentaquark states $P_{c\bar{c}}$, observed by the LHCb Collaboration [69–71], can be generated from baryon–heavy meson interactions [72]. Moreover, it provided a theoretical explanation for the absence of such pentaquark resonances in J/ψ photoproduction observed by the GlueX Collaboration [73,74]. The production mechanisms of hidden-charm pentaquark states with strangeness $S=-1$, reported by the LHC and Belle and Belle II Collaborations [75–77], were also described within this coupled-channel formalism [78], which was further extended to predict double-strangeness hidden-charm pentaquark states [79].

In this work, we investigate the production mechanism for doubly charmed mesons within a coupled-channel formalism. We construct the two-body Feynman kernel amplitudes using effective Lagrangians that respect heavy quark symmetry, chiral symmetry, SU(3) flavor symmetry, and hidden local symmetry. To solve the fully off-shell coupled scattering integral equations, we adopt the BbS scheme, a three-dimensional reduction of the Bethe-Salpeter equation. The dynamically generated resonances appear as either poles on the real axis or in the complex plane of the transition amplitudes. We characterize these tetraquark states by analyzing their pole positions and coupling strengths to the involved channels. We summarize the current results in Fig. 1, which will be discussed in detail.

The structure of the present work is outlined as follows: In Sec. II, we explain the off-shell coupled-channel formalism. In Sec. III, we analyze the kernel amplitudes for various channels, demonstrate the emergence of the $T_{cc}(3875)^+$ state as a DD^* molecular state in the isovector–axial-vector channel by examining the partial-wave transition amplitudes with both positive and negative parities, and predict the existence of three exotic states with $I(J^P)=0(1^+)$, $1(1^+)$, and $0(1^-)$. We discuss their feature by extracting pole positions and coupling strengths and uncertainty asrising from parameters. Finally, in Sec. IV, we summarize the key findings of the current investigation, and draw conclusions.

II. THEORETICAL FRAMEWORK

We start by defining the scattering amplitude as

$$S_{fi}=\delta_{fi}-(2\pi)^4\delta^{(4)}(P_f-P_i)\mathcal{T}_{fi}, \tag{1}$$

where P_i and P_f represent the total four-momenta of the initial and final hadron states, respectively. The transition amplitudes $\mathcal{T}_{fi}$ contains essential information on dynamics of hadronic interactions. They are derived by solving the Bethe-Salpeter (BS) equation

$$\mathcal{T}_{fi}(p,p';s)=\mathcal{V}_{fi}(p,p';s)+\frac{1}{(2\pi)^4}\sum_k\int d^4q\mathcal{V}_{fk}(p,q;s) \times G_k(q;s),\mathcal{T}_{ki}(q,p';s) \tag{2}$$

where p and p' denote the relative four-momenta of the intial and final states, respectively. s stands for the square of the total energy in the center-of-mass (c.m.) frame: $s=P_i^2=P_f^2$. q is the off-mass-shell momentum for the intermediate states in the c.m. frame. $\mathcal{V}_{fi}$ indicates the two-body Feynman kernel amplitudes, which can be constructed by using the effective Lagrangian. The summation runs over intermediate coupled channels involved in the process $f\to i$. The two-body propagator G_i in the off-shell intermediate states is expressed as,

$$G_i=\frac{i}{q_{i1}^2-m_{i1}^2}\frac{i}{q_{i2}^2-m_{i2}^2}. \tag{3}$$

The coupled BS integral equations given in Eq. (2) are illustrated in Fig. 2.

Since it is complicated to deal with the four-dimensional BS equation numerically, we will perform a three-dimensional reduction, following the BbS scheme [63,64] by implementing a specific form of the two-body propagator:

$$G_k(q)=\frac{\pi}{\omega_1^k\omega_2^k}\delta\left(q^0-\frac{\omega_1^k-\omega_2^k}{2}\right)\frac{\omega_1^k+\omega_2^k}{s-(\omega_1^k+\omega_2^k)^2+i\epsilon}, \tag{4}$$

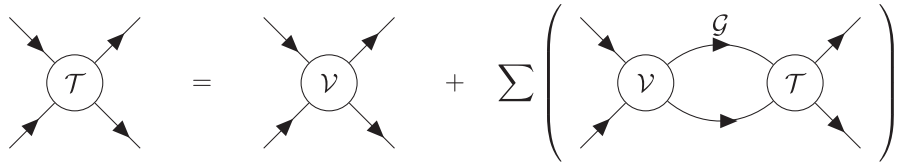


FIG. 2. Graphical representation of the coupled Bethe-Salpeter integral scattering equation.

where $\omega^k_{1(2)} = \sqrt{\boldsymbol{q}^2 + (m^k_{1(2)})^2}$ denotes the on-shell energies for particles 1 and 2 in channel k. Thus, we derive the three-dimensional coupled BbS integral equation expressed as

$$T_{fi}(\boldsymbol{p},\boldsymbol{p}';s) = V_{fi}(\boldsymbol{p},\boldsymbol{p}';s) + \sum_k \int d^3q V_{fk}(\boldsymbol{p},\boldsymbol{q};s)\tilde{G}_k(\boldsymbol{q})T_{ki}(\boldsymbol{q},\boldsymbol{p}';s) \tag{5}$$

with

$$\tilde{G}_k(\boldsymbol{q}) = \frac{1}{(2\pi)^3}\frac{\omega^k_1+\omega^k_2}{2\omega^k_1\omega^k_2}\frac{1}{s-(\omega^k_1+\omega^k_2)^2+i\epsilon}. \tag{6}$$

To clarify the spin-parity assignments for T_{cc} states, we project the $\mathcal{V}$ and $\mathcal{T}$ amplitudes into the partial-wave amplitudes, which results in a one-dimensional coupled partial-wave BbS integral equation,

$$T^{J(fi)}_{\lambda'\lambda}(\mathrm{p},\mathrm{p}';s) = V^{J(fi)}_{\lambda'\lambda}(\mathrm{p},\mathrm{p}';s) + \sum_{\lambda_k}\frac{1}{(2\pi)^3}\int_0^\infty dq \times \frac{\omega^k_1+\omega^k_2}{2\omega^k_1\omega^k_2}\frac{\mathrm{q}^2 V^{J(fk)}_{\lambda'\lambda_k}(\mathrm{p},\mathrm{q};s)T^{J(ki)}_{\lambda'\lambda_k}(\mathrm{q},\mathrm{p}';s)}{s-(\omega^k_1+\omega^k_2)^2+i\epsilon}, \tag{7}$$

where the partial-wave kernel and transition amplitudes V^J and T^J are defined by

$$V^{J(fi)}_{\lambda'\lambda}(\mathrm{p},\mathrm{p}';s) = 2\pi\int d\cos\theta V_{fi}(\mathrm{p},\mathrm{p}',\theta;s)d^J_{\lambda\lambda'}(\theta),$$
$$T^{J(fi)}_{\lambda'\lambda}(\mathrm{p},\mathrm{p}';s) = 2\pi\int d\cos\theta T_{fi}(\mathrm{p},\mathrm{p}',\theta;s)d^J_{\lambda\lambda'}(\theta). \tag{8}$$

Here, $d^J_{\lambda\lambda'}(\cos\theta)$ denotes the reduced Wigner D function and θ is the scattering angle between $\boldsymbol{p}$ and $\boldsymbol{p}'$. Here, $\lambda = \lambda_1 - \lambda_2$ and $\lambda' = \lambda'_1 - \lambda'_2$ indicate the helicity differences between particles 1 and 2 in the initial and final states, respectively. p, p′, and q designate the magnitude of the corresponding three-momenta. We separate the singularity in Eq. (27) arising from the two-body propagator as follows:

$$\mathcal{T}^{J(fi)}_{\lambda'\lambda}(\mathrm{p}',\mathrm{p}) = \mathcal{V}^{J(fi)}_{\lambda'\lambda}(\mathrm{p}',\mathrm{p}) + \frac{1}{(2\pi)^3}\sum_{k,\lambda_k}\left[\int_0^\infty d\mathrm{q}\frac{\mathrm{q}E_k}{E_{k1}E_{k2}}\frac{\mathcal{F}(\mathrm{q})-\mathcal{F}(\tilde{\mathrm{q}}_k)}{s-E_k^2} + \frac{1}{2\sqrt{s}}\left(\ln\left|\frac{\sqrt{s}-E^{\mathrm{thr}}_k}{\sqrt{s}+E^{\mathrm{thr}}_k}\right| - i\pi\right)\mathcal{F}(\tilde{\mathrm{q}}_k)\right] \tag{9}$$

with

$$\mathcal{F}(\mathrm{q}) = \frac{\mathrm{q}}{2}V^{J(fk)}_{\lambda'\lambda_k}(\mathrm{p}',\mathrm{q})T^{J(ki)}_{\lambda_k\lambda}(\mathrm{q},\mathrm{p}), \tag{10}$$

and $\tilde{\mathrm{q}}_k$ denotes the momentum q when $E_{k1}+E_{k2}=\sqrt{s}$. Here, the sign of the imaginary part corresponds to the analytic continuation across the two-body unitarity cut. The factor $-i\pi$ in Eq. (9) thus indicates that we move to the unphysical Riemann sheet associated with the branch point $\tilde{\mathrm{q}}_k$, since the pole of the two-body propagator in channel k lies on the lower half of the complex plane. Conversely, the physical Riemann sheet is reached by taking $+i\pi$.

To construct the two-body Feynman kernel amplitudes, we employ the effective Lagrangians for D and D^* mesons, considering heavy-quark spin-flavor symmetry, SU(3) flavor symmetry, chiral symmetry, and hidden local symmetry. In the $m_Q \to \infty$ limit, the effective Lagrangian can be written as

$$\mathcal{L}^Q_{\mathrm{heavy}} = ig\mathrm{Tr}[H_b\gamma_\mu\gamma_5\mathcal{A}^\mu_{ba}\bar{H}_a] + i\beta\mathrm{tr}[H_b v_\mu(\mathcal{V}-\rho)^\mu_{ba}\bar{H}_a] + i\lambda\mathrm{tr}[H_b\sigma_{\mu\nu}F^{\mu\nu}_{ba}\bar{H}_a] + g_\sigma H_a H_a\sigma, \tag{11}$$

where H_a denotes a superfield consisting of the pseudoscalar and vector heavy meson fields P and P^*_μ

$$H_a = \frac{1+\not{v}}{2}[\not{P}^*_a - P_a\gamma_5] \tag{12}$$

in 4×4 Dirac space. The superfield preserves the heavy quark spin-flavor symmetry and satisfies $\not{v}H = H$. The limit $m_Q \to \infty$ requires the field normalization to be

$$\langle 0|P_a|(Q\bar{q})_a, 0^-\rangle = \sqrt{M_H},$$
$$\langle 0|P^{*\mu}_a|(Q\bar{q})_a, 1^-\rangle = \epsilon^\mu\sqrt{M_H}, \tag{13}$$

with the polarization vector of the vector heavy meson, ϵ^μ. The conjugate field is then expressed as

$$\bar{H}_a = \gamma^0 H_a^\dagger \gamma^0 = [\not{P}_a^{*\dagger} + P_a^\dagger \gamma_5]\frac{1+\not{v}}{2}. \tag{14}$$

The heavy quark flavor symmetry allows $P^{(*)}$ to be either $P^{(*)} = \{D^{(*)0}(c\bar{u}), D^{(*)+}(c\bar{d}), D_s^{(*)+}(c\bar{s})\}$ for $Q = c$ or $P^{(*)} = \{B^{(*)-}(b\bar{u}), B^{(*)0}(b\bar{d}), B_s^{(*)0}(b\bar{s})\}$ for $Q = b$.

The matter fields H_a interact with Goldstone bosons via the chiral transformation $H \to HU^\dagger$. The Goldstone fields appear as the coset field ξ of $\mathrm{SU}(3)_L \times \mathrm{SU}(3)_R/\mathrm{SU}(3)_V$ [80,81],

$$\xi(x) = e^{i\mathcal{M}(x)/f_\pi}, \quad \text{with}$$
$$\mathcal{M} = \begin{pmatrix} \frac{\pi^0}{\sqrt{2}} + \frac{\eta}{\sqrt{6}} & \pi^+ & K^+ \\ \pi^- & -\frac{\pi^0}{\sqrt{2}} + \frac{\eta}{\sqrt{6}} & K^0 \\ K^- & \bar{K}^0 & -\sqrt{\frac{2}{3}}\eta \end{pmatrix}, \tag{15}$$

where $f_\pi = 132$ MeV is the pion decay constant. The axial-vector and vector currents are then constructed from the ξ field,

$$\mathcal{A}^\mu = \frac{1}{2}(\xi^\dagger \partial^\mu \xi - \xi \partial^\mu \xi^\dagger) = \frac{i}{f_\pi}\partial^\mu \mathcal{M} + \cdots,$$
$$\mathcal{V}^\mu = \frac{1}{2}(\xi^\dagger \partial^\mu \xi + \xi \partial^\mu \xi^\dagger) = \frac{i}{2f_\pi^2}[\mathcal{M}, \partial^\mu \mathcal{M}] + \cdots, \tag{16}$$

which transform under U as

$$\mathcal{A}^\mu \to U\mathcal{A}^\mu U^\dagger,$$
$$\mathcal{V}^\mu \to U\mathcal{V}^\mu U^\dagger - \partial^\mu U U^\dagger. \tag{17}$$

Thus, the effective chiral Lagrangians for the $\mathcal{M}PP^*$ and $\mathcal{M}P^*P^*$ vertices can be constructed as follows

$$\mathcal{L}_{PP^*\mathcal{M}} = -\frac{2g}{f_\pi} P_a^{Q\dagger} \partial^\mu \mathcal{M}_{ba} P_{b\mu}^{Q^*} + \text{H.c.},$$
$$\mathcal{L}_{P^*P^*\mathcal{M}} = -\frac{2ig}{f_\pi} \epsilon^{\mu\nu\alpha\beta} P_{a\alpha}^{Q^*\dagger} v_\beta \partial_\mu \mathcal{M}_{ba} P_{b\nu}^{Q^*}. \tag{18}$$

The interaction for the vector meson octet is established via hidden local symmetry. A gauge equivalence between $\mathrm{SU}(3)_L \times \mathrm{SU}(3)_R/\mathrm{SU}(3)_V$ and $\mathrm{SU}(3)_L \times \mathrm{SU}(3)_R \times [\mathrm{SU}(3)_V]_{\text{local}}$ allows the emergence of the vector mesons as dynamical gauge bosons of hidden local symmetry [82,83]. The vector meson octet is then given by

$$\rho^\mu = i\frac{g_V}{\sqrt{2}} V^\mu, \quad V^\mu = \begin{pmatrix} \frac{\rho^0}{\sqrt{2}} + \frac{\omega}{\sqrt{2}} & \rho^+ & K^{*+} \\ \rho^- & -\frac{\rho^0}{\sqrt{2}} + \frac{\omega}{\sqrt{2}} & K^{*0} \\ K^{*-} & \bar{K}^{*0} & \phi \end{pmatrix}^\mu. \tag{19}$$

The corresponding field strength tensor is defined as $F^{\mu\nu} = \partial^\mu \rho^\nu - \partial^\nu \rho^\mu + [\rho^\mu, \rho^\nu]$, which gives rise to the tensor interaction term in Eq. (11). Therefore, the effective Lagrangians for the PPV, P^*P^*V, and PP^*V vertices are expressed as

$$\mathcal{L}_{PPV} = -\sqrt{2}\beta g_V P_a^\dagger v_\mu V_{ba}^\mu P_b,$$
$$\mathcal{L}_{P^*P^*V} = \sqrt{2}\beta g_V P_{a\nu}^{*\dagger} v_\mu V_{ba}^\mu P_b^{*\nu} + 2\sqrt{2} i\lambda g_V P_{a\mu}^{*\dagger} P_{b\nu}^* V_{ba}^{\mu\nu},$$
$$\mathcal{L}_{PP^*V} = -2\sqrt{2}\lambda g_V \varepsilon_{\beta\alpha\mu\nu}(P_a^\dagger v^\beta P_b^{*\alpha} + P_a^{*\dagger\alpha} v^\beta P_b)(\partial^\mu V^\nu)_{ba}, \tag{20}$$

where the heavy quark velocity can be replaced by $i\overleftrightarrow{\partial}_\mu/(2\sqrt{MM'}) = i(\overleftarrow{\partial} - \overrightarrow{\partial})/(2\sqrt{MM'})$, with $M^{(\prime)}$ denoting the mass of the heavy meson. The effective Lagrangians for the scalar meson σ are obtained as

$$\mathcal{L}_{PP\sigma} = -2g_{PP\sigma} P_a^\dagger P_a \sigma,$$
$$\mathcal{L}_{P^*P^*\sigma} = 2g_{P^*P^*\sigma} P_{a\mu}^{*\dagger} P_a^{*\mu} \sigma. \tag{21}$$

We now proceed to determine the coupling constants in the effective Lagrangians. The value of g in Eq. (18) is fixed by the partial decay width of $D^{*+} \to D^0\pi^+$ [84],

$$\Gamma(D^{*+} \to D^0\pi^+) = \frac{g^2}{6\pi f_\pi^2}|\boldsymbol{p}_\pi|^3, \tag{22}$$

which yields $g = 0.59$. The value of $\beta = 0.9$ in Eq. (20) is determined by using the vector meson dominance [82]. The value of $\beta = 0.9$ in Eq. (20) is determined by using vector meson dominance [82], and $\lambda = 0.56\ \mathrm{GeV}^{-1}$ is fixed phenomenologically by the $B \to K^*$ transition form factor at high q^2 [85,86].

For the σPP and σP^*P^* coupling constants, the σ meson was often assumed to be a chiral partner of the pion, leading to the relation $g_\sigma = g_\pi/(2\sqrt{6})$. Moreover, it was assumed that $g_{\sigma P^*P^*}$ equals $g_{\sigma PP}$. However, due to the large width of the σ meson [also known as $f_0(500)$] [87], it is more plausible to consider the σ exchange as a correlated 2π exchange in S wave. There is no fundamental reason to require $g_{\sigma PP} = g_{\sigma P^*P^*}$. In Ref. [88], the coupling constants $g_{\sigma PP}$ and $g_{\sigma P^*P^*}$ were determined by using dispersion relations within this theoretical framework. For the charmed mesons, we obtained the following results: $g_{\sigma DD} = 1.50$ and $g_{\sigma D^*D^*} = 5.21$. Since the ρ-meson exchange is regarded as correlated 2π exchange in P wave, we similarly determine $g_{\rho DD} = 1.65$ and $g_{\rho D^*D^*} = 6.47$. The ρDD^* coupling constant is fixed at $g_{\rho DD^*} = 5.8$ using the relation $g_V = m_\rho/f_\pi$ from the Kawarabayashi-Suzuki-Riazuddin-Fayyazuddin relation [89,90].

Since the mass of $T_{cc}(3875)^+$ is found to be below the D^0D^{*+} threshold, we consider three channels, namely, DD, DD^*, and D^*D^*. The kernel matrices are therefore constructed as,

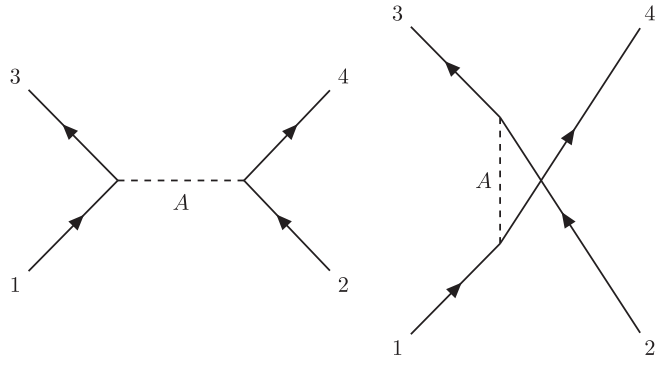


FIG. 3. t- and u-channel Feynman diagrams.

$$\mathcal{V} = \begin{pmatrix} \mathcal{V}_{DD\to DD} & \mathcal{V}_{DD\to DD^*} & \mathcal{V}_{DD\to D^*D^*} \\ \mathcal{V}_{DD^*\to DD} & \mathcal{V}_{DD^*\to DD^*} & \mathcal{V}_{DD^*\to D^*D^*} \\ \mathcal{V}_{D^*D^*\to DD} & \mathcal{V}_{D^*D^*\to DD^*} & \mathcal{V}_{D^*D^*\to D^*D^*} \end{pmatrix}, \quad (23)$$

where each matrix element is expressed in terms of the initial and final momenta, p and p′. The kernel amplitudes are derived as the sum of the Feynman amplitudes in the t and u channels at tree level,

$$\mathcal{V}_{i\to j} = \sum_A \mathcal{M}^A_{i\to j}, \quad (24)$$

where A represents all possible particle exchanges for the process $i \to j$. Note that s-channel pole diagrams are not included since we focus on the dynamical generation of resonances. Figure 3 depicts generic diagrams for the t and u channels.

The Feynman kernel amplitude for the exchange of a particle A has the structure

$$\mathcal{M}^A_{i\to j} = \mathrm{IS} F_A^2 \Gamma_1^A \mathcal{P}^A \Gamma_2^A, \quad (25)$$

where IS denotes the isospin factor derived from the SU(3) Clebsch-Gordan coefficients. In this expression, Γ_1^A (Γ_2^A) is the vertex function for the initial (final) state, and $\mathcal{P}^A$ is the propagator of the exchanged particle A. A form factor F_A is introduced at each vertex to account for the finite size of the corresponding hadron and to ensure the unitarity of the transition amplitudes. We choose the form factor as

$$F_A(q^2) = \left(\frac{n\Lambda^2 - m_A^2}{n\Lambda^2 - q^2}\right)^n, \quad (26)$$

where Λ is the cutoff mass, m_A is the mass of the exchanged particle, and q denotes the momentum transfer between the incoming and outgoing states. In the limit $n \to \infty$, F_A reduces to a Gaussian form. In this work, we fix $n = 2$, since the results are not sensitive to this choice.

The cutoff masses are the main source of uncertainty because they cannot be precisely determined due to the lack of experimental data. To minimize these uncertainties, we adopt the idea that heavier hadrons are more compact than lighter ones [91–93], so that the cutoff mass can be regarded as the inverse of the particle size. Consequently, it increases monotonically with the mass of the exchanged particle. Based on this, we define the reduced cutoff mass Λ_0 as $\Lambda_0 \equiv \Lambda - m_{\mathrm{ex}} \approx (600\text{–}700)$ MeV. This strategy has the benefit of eliminating the need to fit each cutoff mass individually. This approach has been phenomenologically successful in describing various hadronic processes [65,66,88], particularly those involving heavy hadrons [66,68,88]. In the present work, we fix the reduced cutoff mass to $\Lambda_0 = 600$ MeV and examine how the doubly charmed tetraquark resonances arise. Note that this value is not fitted to the existing data on $T_{cc}(3875)$. The uncertainty due to Λ_0 is discussed by varying it within ± 100 MeV in Sec. III. The values of the various IS factors and Λ_0 for the isoscalar and isovector channels are listed in Tables I and II, respectively.

The invariant amplitudes for pseudoscalar exchanges are given by

$$\mathcal{M}^{\mathcal{M}}_{P^*P\to P^*P} = -\mathrm{IS} F_{\mathcal{M}}^2 \frac{4g^2}{f_\pi^2} \frac{(\epsilon_1\cdot q)(\epsilon_3^*\cdot q)}{q^2 - m_{\mathcal{M}}^2},$$
$$\mathcal{M}^{\mathcal{M}}_{P^*P^*\to P^*P^*} = -\mathrm{IS} F_{\mathcal{M}}^2 \frac{g^2}{f_\pi^2} \varepsilon_{\mu\nu\alpha\beta}\varepsilon^{\lambda\kappa\rho\sigma} \frac{q^\mu (p_1+p_3)^\beta q_\lambda (p_2+p_4)_\sigma \epsilon_1^\nu \epsilon_2^\alpha \epsilon_3^{*\kappa} \epsilon_4^{*\rho}}{q^2 - m_{\mathcal{M}}^2}. \quad (27)$$

Those for vector-meson exchanges are written as

$$\mathcal{M}^V_{PP\to PP} = \mathrm{IS} F_V^2 \frac{\beta^2 g_V^2}{2} \frac{(p_1+p_3)\cdot(p_2+p_4) - ((p_1+p_3)\cdot q)((p_2+p_4)\cdot q)/m_V^2}{q^2 - m_V^2},$$
$$\mathcal{M}^V_{P^*P\to P^*P} = \mathrm{IS} F_V^2 \lambda\beta g_V^2 \varepsilon_{\beta\alpha\mu\nu}(p_1+p_3)^\beta q^\mu \frac{g^{\nu\sigma} - q^\nu q^\sigma/m_V^2}{q^2 - m_V^2}(p_2+p_4)_\sigma \epsilon_1^\alpha \epsilon_3^*,$$
$$\mathcal{M}^V_{P^*P^*\to P^*P^*} = -\mathrm{IS} F_V^2 g^2_{P^*P^*V} \frac{1}{q^2 - m_V^2}[(p_1+k_1)\cdot(p_2+k_2)(\epsilon_1\cdot\epsilon_3^*)(\epsilon_2\cdot\epsilon_4^*) - (\epsilon_1\cdot\epsilon_4^*)(\epsilon_2\cdot\epsilon_3^*)((p_1-k_1)\cdot(p_2-k_2))]. \quad (28)$$

TABLE I. Values of the IS factors and reduced cutoff masses for each vertex and isospin factor for the kernel amplitudes for DD, DD^* and D^*D^* in the isoscalar ($I = 0$) channel.

Reaction	Exchange	IS factor		Λ_0 (MeV)
		t channel	u channel	
$DD \to DD$	σ	1	-1	600
	ρ	$-3/2$	$3/2$	600
	ω	$1/2$	$-1/2$	600
$DD \to DD^*$	ρ	$-3/2$	$3/2$	600
	ω	$1/2$	$-1/2$	600
$DD \to D^*D^*$	π	$\cdots$	$3/2$	600
	η	$\cdots$	$-1/6$	600
	ρ	$-3/2$	$3/2$	600
	ω	$1/2$	$-1/2$	600
$DD^* \to DD^*$	σ	1	$\cdots$	600
	π	$\cdots$	$3/2$	600
	η	$\cdots$	$-1/6$	600
	ρ	$-3/2$	$3/2$	600
	ω	$1/2$	$-1/2$	600
$DD^* \to D^*D^*$	π	$-3/2$	$3/2$	600
	η	$1/6$	$-1/6$	600
	ρ	$-3/2$	$3/2$	600
	ω	$1/2$	$-1/2$	600
$D^*D^* \to D^*D^*$	σ	1	-1	600
	π	$-3/2$	$3/2$	600
	η	$1/6$	$-1/6$	600
	ρ	$-3/2$	$3/2$	600
	ω	$1/2$	$-1/2$	600

TABLE II. Values of the IS factors and reduced cutoff masses for each vertex and isospin factor for the kernel amplitudes for DD, DD^*, and D^*D^* in the isovector ($I = 1$) channel.

Reaction	Exchange	IS factor		Λ_0 (MeV)
		t channel	u channel	
$DD \to DD$	σ	1	$\cdots$	600
	ρ	$1/2$	$1/2$	600
	ω	$1/2$	$1/2$	600
$DD \to DD^*$	ρ	$1/2$	$1/2$	600
	ω	$1/2$	$1/2$	600
$DD \to D^*D^*$	π	$\cdots$	$1/2$	600
	η	$\cdots$	$1/6$	600
	ρ	$1/2$	$1/2$	600
	ω	$1/2$	$1/2$	600
$DD^* \to DD^*$	σ	1	$\cdots$	600
	π	$\cdots$	$1/2$	600
	η	$\cdots$	$1/6$	600
	ρ	$1/2$	$1/2$	600
	ω	$1/2$	$1/2$	600
$DD^* \to D^*D^*$	π	$1/2$	$1/2$	600
	η	$1/6$	$1/6$	600
	ρ	$1/2$	$1/2$	600
	ω	$1/2$	$1/2$	600
$D^*D^* \to D^*D^*$	σ	1	$\cdots$	600
	π	$1/2$	$1/2$	600
	η	$1/6$	$1/6$	600
	ρ	$1/2$	$1/2$	600
	ω	$1/2$	$1/2$	600

III. RESULTS AND DISCUSSION

While the parity of the $T_{cc}(3875)$ is known to be positive, we will show that tetraquark states with both positive and negative parities are dynamically generated. Since we are mainly concerned with their production mechanism, we do not fit the experimental data by adjusting parameters such as coupling constants and reduced cutoff masses. We begin by discussing the partial-wave kernel amplitudes. Interestingly, three bound states emerge even at the level of single channels. Once coupled channels are introduced, the positions of the bound states shift either along the real axis or into the complex plane, and an additional resonance appears above the D^*D^* threshold with negative parity. This will be discussed in the subsection on transition amplitudes. We then examine the pole positions of the tetraquark resonances and their coupling strengths to each channel. Finally, we investigate the uncertainties that arise from varying the values of the reduced cutoff mass.

A. Kernel amplitudes

The kernel amplitudes are determined by the Feynman invariant amplitudes given in Eqs. (27) and (28). To generate resonances, it is essential to have attractive interactions in the kernel amplitudes. By examining the partial-wave kernel amplitudes, we can understand how the tetraquark resonances are generated.

1. Positive parity

In the upper panel of Fig. 4, we present the numerical results for the DD and D^*D^* partial-wave kernel amplitudes $\mathcal{V}^J_{ij}$ for the isoscalar-scalar channel ($I = 0$, $J = 0$). Since the contributions from partial-wave amplitudes higher than the P wave are found to be negligible, we focus on the scalar (S-wave) kernel amplitudes for the

TABLE III. Coupling strengths g_i for exotic mesons T_{cc}, labeled by the real part of the pole positions.

$I(J^P)$	$0(1^+)$		$1(1^+)$	$0(1^-)$
State	$T_{cc}^{I=0}(3823)$	$T_{cc}^{I=0}(4102)$	$T_{cc}^{I=1}(3875)$	$T_{cc}^{I=0}(4090)$
$\sqrt{s_R}$ [MeV]	3823.058	$4102.326 - i83.044$	3875.677	$4089.67 - i41.88$
$g_{DD(^1P_1)}$	⋯	⋯	⋯	$4.834 - i2.214$
$g_{DD^*(^3S_1)}$	17.95	$1.310 + i1.045$	3.276	⋯
$g_{DD^*(^3D_1)}$	0.113	$0.106 + i0.2113$	1.342×10^{-3}	⋯
$g_{DD^*(^3P_1)}$	⋯	⋯	⋯	$0.289 + i2.035$
$g_{D^*D^*(^3S_1)}$	24.97	$0.299 + i1.310$	2.147×10^{-2}	⋯
$g_{D^*D^*(^3D_1)}$	0.589	$0.148 + i0.5503$	3.794×10^{-4}	⋯
$g_{D^*D^*(^5D_1)}$	3.325×10^{-4}	$(4.800 + i2.246) \times 10^{-3}$	4.446×10^{-4}	⋯
$g_{D^*D^*(^1P_1)}$	⋯	⋯	⋯	$2.331 - i7.371$
$g_{D^*D^*(^3P_1)}$	⋯	⋯	⋯	$(2.624 + i1.751) \times 10^{-3}$
$g_{D^*D^*(^5P_1)}$	⋯	⋯	⋯	$4.110 - i1.168$
$g_{D^*D^*(^5F_1)}$	⋯	⋯	⋯	$1.707 - i0.732$

positive-parity channels. Note that the P-wave amplitudes are not considered because of the parity in this subsection. In the upper-left panel of Fig. 4, we display the individual meson-exchange terms. The u-channel ρ exchange, the t-channel ω exchange, and the u-channel σ exchange yield repulsive effects, whereas the t-channel ρ exchange, the u-channel ω exchange, and the t-channel σ exchange provide attraction. Consequently, the total elastic DD kernel amplitude is weakly repulsive and small over the entire range of the c.m. energy, so it cannot generate any resonance. In the upper-right panel of Fig. 4, we present the results for the $D^*D^* \to D^*D^*$ partial-wave kernel amplitudes, which show behavior similar to the corresponding $DD \to DD$ case. Interestingly, the π-exchange diagrams

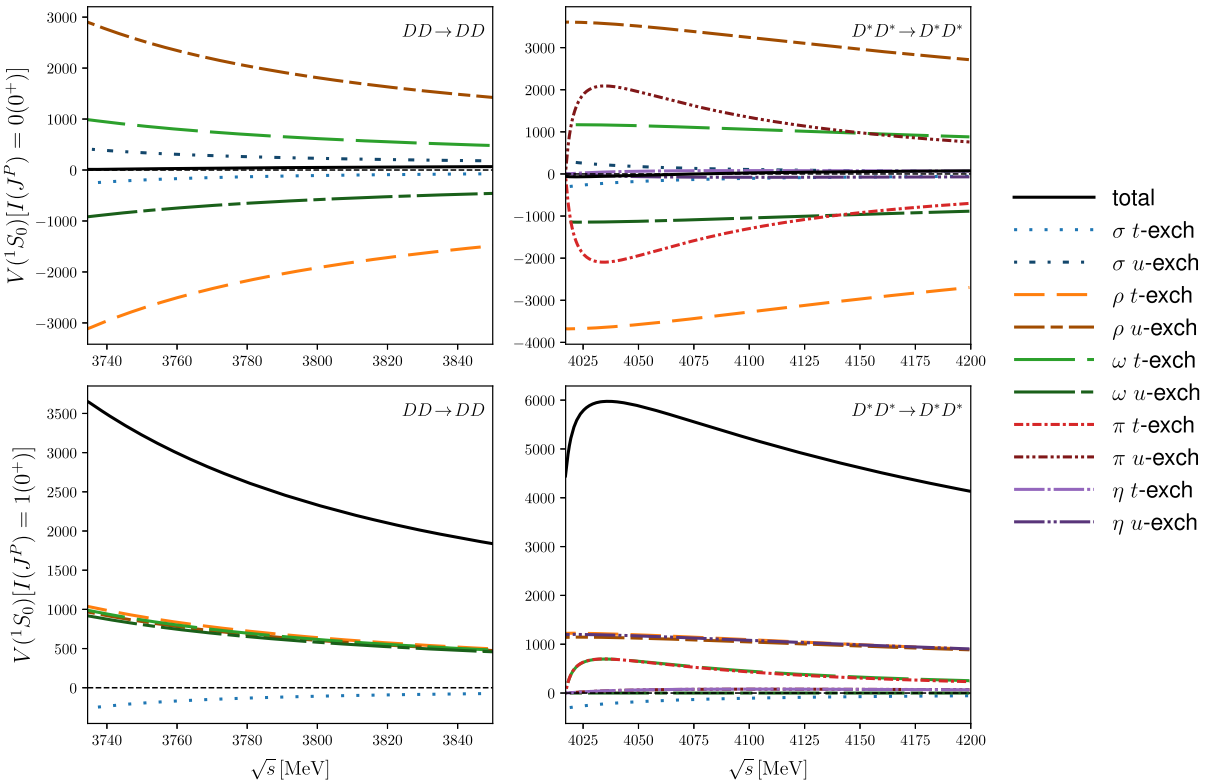


FIG. 4. Scalar kernel amplitudes for the diagonal elements, i.e., $DD \to DD$, as functions of $\sqrt{s}$. The upper panels depict the results for those with $I = 0$ and $J = 0$, whereas the lower panels show the results for those with $I = 1$ and $J = 0$.

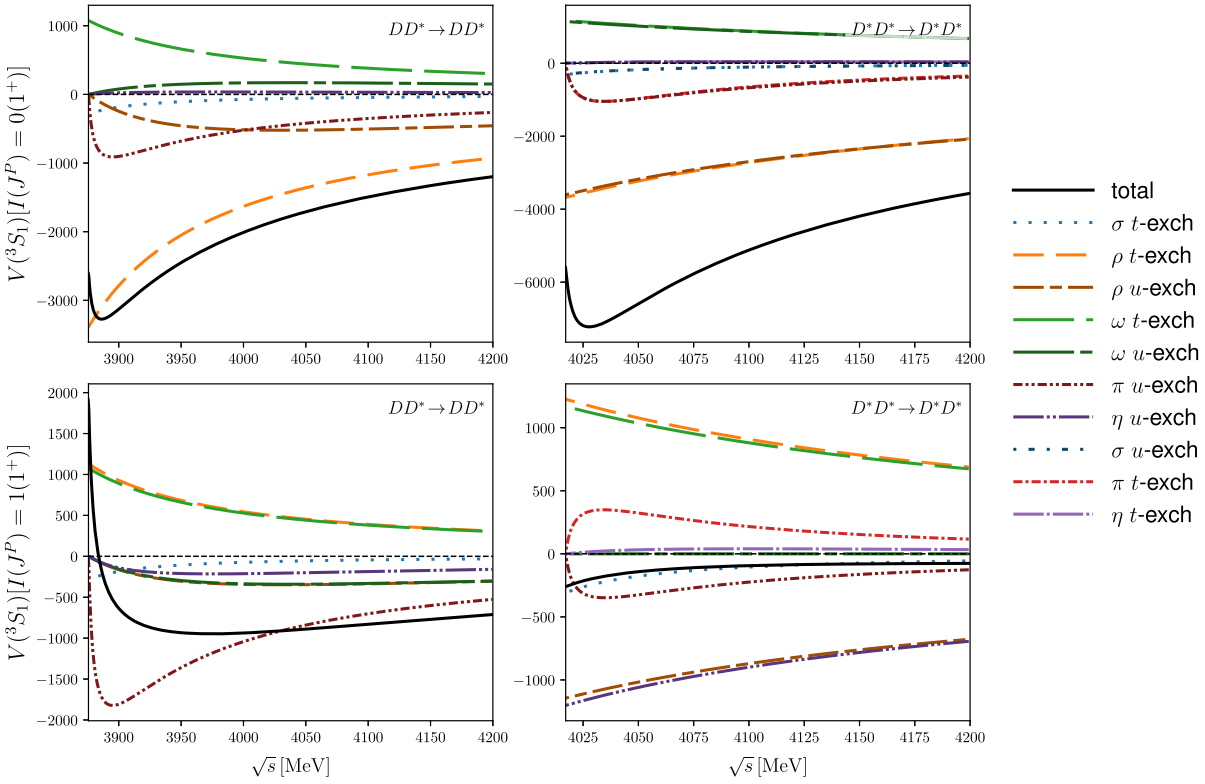


FIG. 5. Axial-vector ($J^P = 1^+$) elastic kernel amplitudes as functions of $\sqrt{s}$. The upper panels depict the results for those with $I = 0$ and $J = 1$, whereas the lower panels show the results for those with $I = 1$ and $J = 1$.

exhibit a different energy dependence; nevertheless, the t-channel part is almost canceled by the u-channel part. The η-meson effect is negligible. As a result, the total elastic D^*D^* kernel amplitude is also negligibly small.

In the lower-left panel of Fig. 4, we draw the results for the DD partial-wave kernel amplitudes in the isovector-scalar channel. We find that almost all meson-exchange diagrams are repulsive, except for the t-channel σ exchange. Thus, the corresponding total kernel amplitude does not produce any resonance. Similarly, the D^*D^* kernel amplitudes in the same channel are also repulsive, as shown in the lower-right panel.

In Fig. 5, on the other hand, the kernel amplitudes in the $J = 1$ channel provide strong attractions, which are crucial for generating tetraquark resonances. The upper panels of Fig. 5 show that the elastic isoscalar–axial-vector ($I = 0$, $J^P = 1^+$) DD^* and D^*D^* amplitudes are negative due to dominant attraction from ρ and π exchange. This leads to the formation of two bound states in the isoscalar–axial-vector channel. In the lower panels of Fig. 5, we present the isovector–axial-vector kernel amplitudes. While the overall behavior is similar to that of the isoscalar–axial-vector channel, the elastic DD^* amplitude becomes the most dominant. Therefore, a bound state also arises in the DD^* channel. It is noteworthy that the $DD^* \to D^*D^*$ transition amplitude nearly vanishes although we do not provide off-diagonal elements. This comes from the fact that the ρ- and ω-exchange terms almost cancel each other due to the different signs of the IS factor as shown in the lower-right panel of Fig. 5.

2. Negative parity

The $^3P_0$ channel with $J = 0$, as well as the $^1P_1$ and $^3P_1$ channels with $J = 1$, are responsible for the negative-parity resonances. In Fig. 6, the P-wave kernel amplitudes are illustrated in the LSJ basis. In the $J = 0$ channel, the conservation of total angular momentum requires $S = 1$, so that the elastic DD kernel amplitude must vanish. Interestingly, vector meson exchanges are rather small in the $^3P_0$ channel, so that the π exchanges give dominant attraction near the thresholds. The elastic DD^* kernel amplitude dominates over all other amplitudes and provides a strong attraction. The elastic D^*D^* amplitude is negligible, since the contribution from the π exchange in the u channel is almost canceled by that in the t channel. Similar features are observed in the $J = 1$ channel, where the elastic DD^* and D^*D^* amplitudes dominate over the transition ones. Although the corresponding kernel amplitudes exhibit negative bump structures, bound states do not appear in the negative-parity case.

The upper and lower panels of Fig. 7 show the results for the P-wave $^1P_1$ and $^3P_1$ kernel amplitudes with $J = 1$, respectively. The isoscalar $^1P_1$ amplitudes, displayed in the

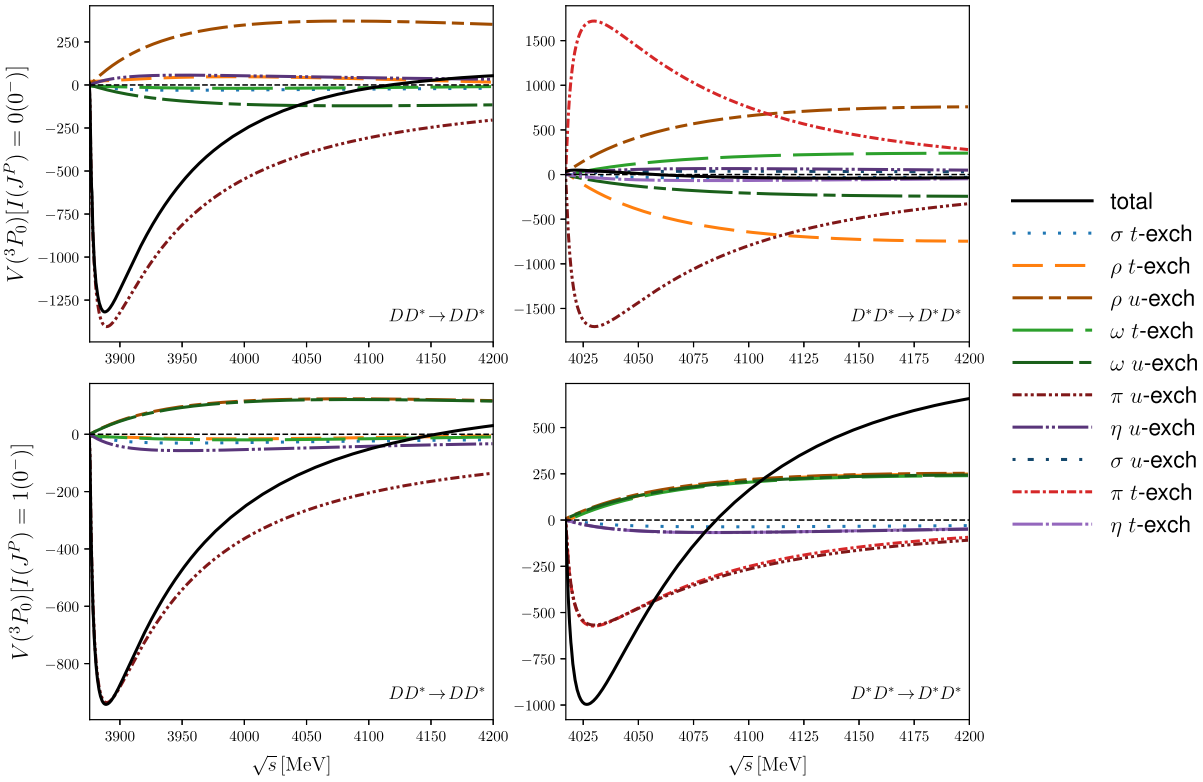


FIG. 6. Pseudoscalar ($J^P = 0^-$) elastic kernel amplitudes as functions of $\sqrt{s}$. The upper panels depict the results for those with $I = 0$ and $J = 0$, whereas the lower panels shows the results for those with $I = 1$ and $J = 0$.

upper panels of Fig. 7, are much larger than the other P-wave amplitudes. While they are mostly attractive, they do not lead to the formation of bound states. Therefore, the negative-parity kernel amplitudes are conclusively not strong enough to generate tetraquark bound states.

B. Transition amplitudes

We are now in a position to discuss the results for the transition amplitudes. The partial-wave transition amplitudes are obtained by solving Eq. (7), which indicates that all the channels are coupled to each other. To understand the behavior of the coupled transition amplitudes, it is worthwhile to examine each single channel separately. Thus, we first scrutinize a single channel by switching off the other channels in Eq. (7), and then continue to investigate the features of the fully coupled transition amplitudes. When we consider single channels with $J = 0$, we do not find any bound states. For $J = 1$, we observe three bound states. It is important to note that only when all channels are coupled does one of them become a resonance in the complex plane. The other two bound states are shifted due to the coupled-channel effects.

1. Positive parity

We first examine the elastic DD^* single channel. In the left and right panels of Fig. 8, we clearly see that the S-wave amplitudes $T_{DD^*\to DD^*}(I = 0, J = 1)$ and $T_{DD^*\to DD^*}(I = 1, J = 1)$ exhibit bound-state structures near the DD^* mass threshold at $\sqrt{s} = 3875.81$ MeV. As shown in Fig. 5, the DD^* kernel amplitudes provide strong attractions, which lead to the generation of two bound states slightly below the threshold in the $^3S_1$ channels, corresponding to different isospins. We also predict the isovector bound state, as demonstrated in the right panel of Fig. 8.

Figure 9 presents the results for the single-channel $D^*D^* \to D^*D^*$ transition amplitudes. The left panel shows the results for the isoscalar channel ($I = 0$), whereas the right one displays those for the isovector channel ($I = 1$). In the isoscalar case, a deep bound state is generated significantly below the D^*D^* mass threshold. The corresponding pole is located at $\sqrt{s} = 3962.55$ MeV, implying a binding energy of approximately 54.57 MeV relative to the threshold. This strong attraction in the D^*D^* elastic channel is consistent with the kernel amplitude results shown in Fig. 5 for $J = 1$ and $I = 0$. In contrast, the isovector channel does not exhibit any bound-state structure near the D^*D^* threshold. Thus, no bound state or resonance is found in the D^*D^* channel with $I = 1$ within the present framework.

We now scrutinize the coupled-channel effects on the elastic DD^* and D^*D^* interactions. Figure 10 shows the coupled-channel transition amplitudes in the $^3S_1$ channels with isospin $I = 0$ (left panel) and $I = 1$ (right panel) as

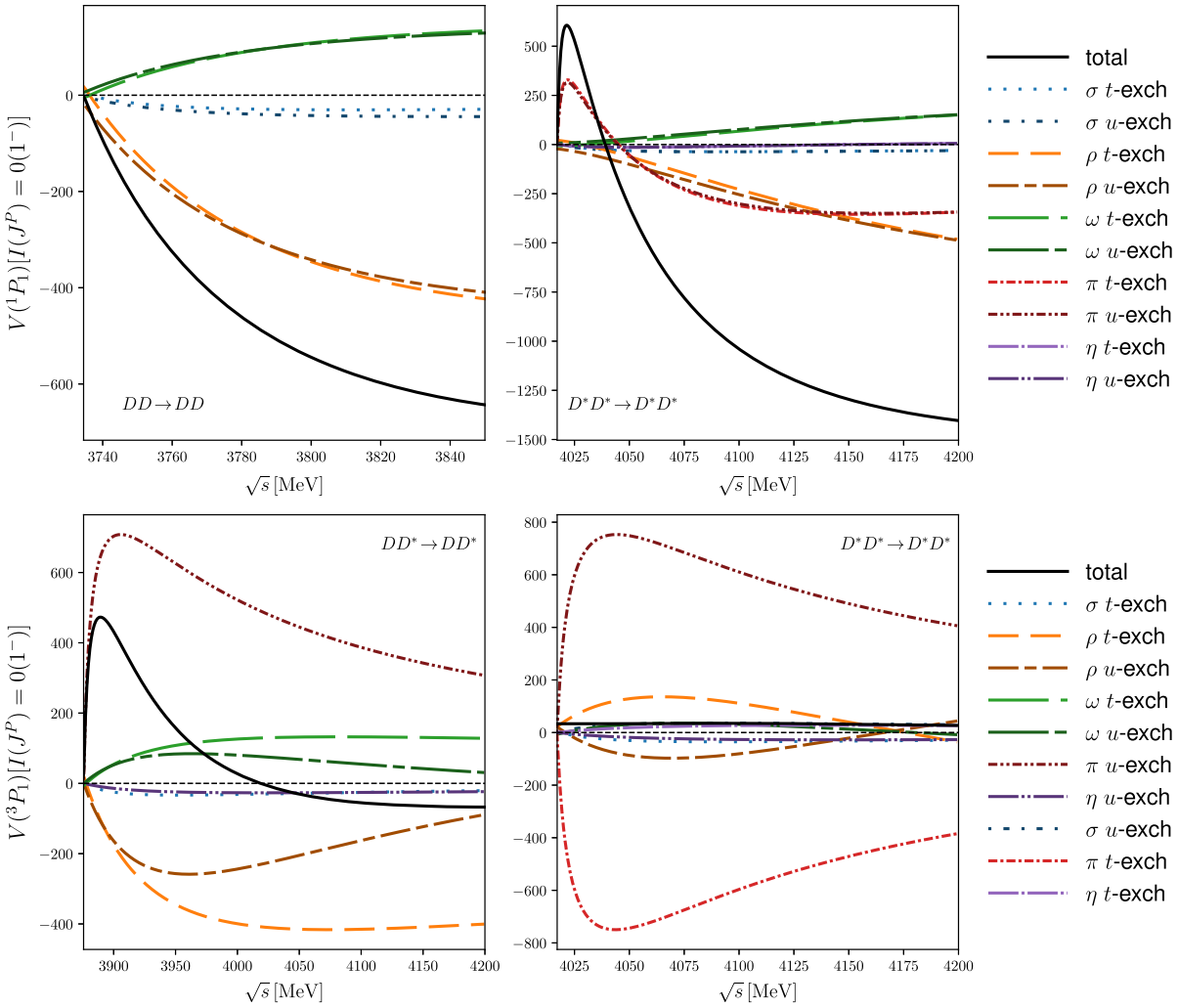


FIG. 7. Vector ($J^P = 1^-$) elastic kernel amplitudes as functions of $\sqrt{s}$. The left panel depicts the results for those with $I = 0$ and $J = 1$, whereas the right panel shows the results for those with $I = 1$ and $J = 1$.

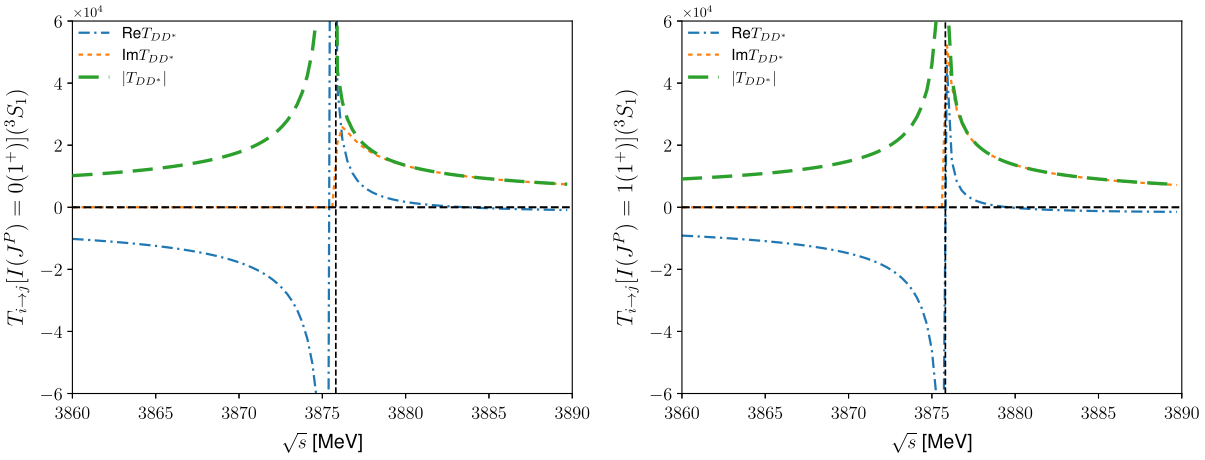


FIG. 8. Single-channel transition amplitudes for elastic DD^* scattering in the $^3S_1$ channels with isospin $I = 0$ (left panel) and $I = 1$ (right panel) as functions of the c.m. energy. The vertical dashed lines indicate the DD^* threshold.

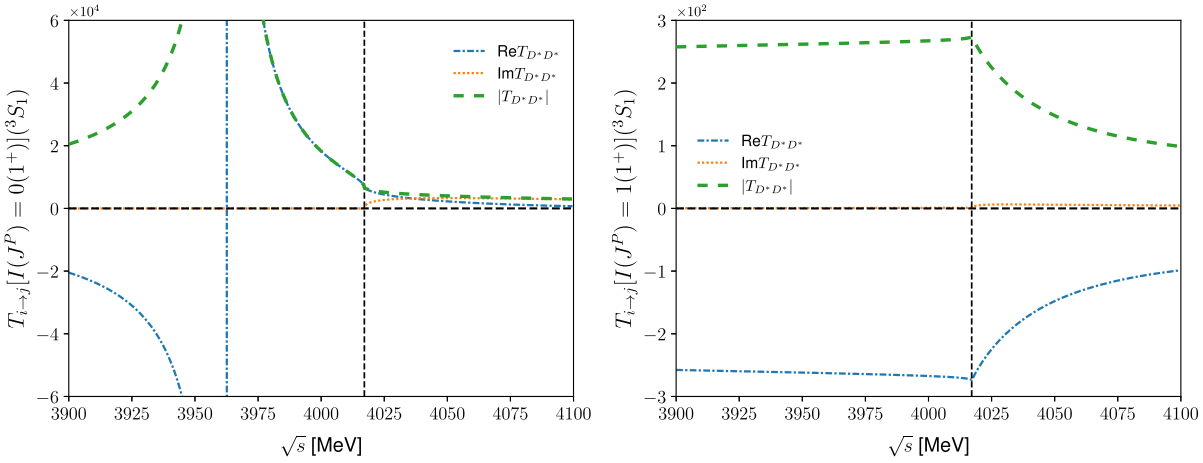


FIG. 9. Single-channel transition amplitudes for elastic D^*D^* scattering in the $^3S_1$ channels with isospin $I=0$ (left panel) and $I=1$ (right panel) as functions of the c.m. energy. The vertical dashed lines indicate the D^*D^* threshold.

functions of the c.m. energy. In the isoscalar channel, a pole appears as a result of the combined attractions in the DD^* and D^*D^* channels. The attractive kernel amplitudes compete with the repulsive one in the $DD^*\to D^*D^*$ transition, as shown in Fig. 5. Consequently, the pole becomes more deeply bound than in the single-channel case, with a binding energy of approximately 58 MeV. Since the DD threshold is absent in this S-wave channel, there is no open channel below the DD^* threshold. As a result, we find a bound state instead of a resonance. Had we considered three-body channels such as the $DD\pi$ channel, the bound state would have moved to the complex plane.

Interestingly, the bound state that existed in the D^*D^* channel, initially located between the DD^* and D^*D^* thresholds, disappears in the fully coupled transition amplitude as a result of the DD^* coupled-channel effect. The isovector bound state, on the other hand, remains largely unaffected by the D^*D^* potential and appears close to the DD^* threshold, with a binding energy of about 10 keV. Turning on the full coupled-channel effects, we observe that the bound state around 3960 MeV in the D^*D^* single channel (see Fig. 9) evolves into a resonance, with the pole position located at 4102 MeV and a decay width of 166 MeV. This indicates that the effects of the $DD^*\to DD^*$ and $DD^*\to D^*D^*$ channels are crucial in predicting this resonance state.

2. Negative parity

As shown in the left panel of Fig. 7, the kernel amplitudes for the $^1P_1$ channels are mostly attractive. This leads us to expect bound states even in the single-channel transition amplitudes with negative parity. However, none of the single-channel T amplitudes exhibit any indication of such states. When we consider the full coupled-channel case, however, a resonance emerges.

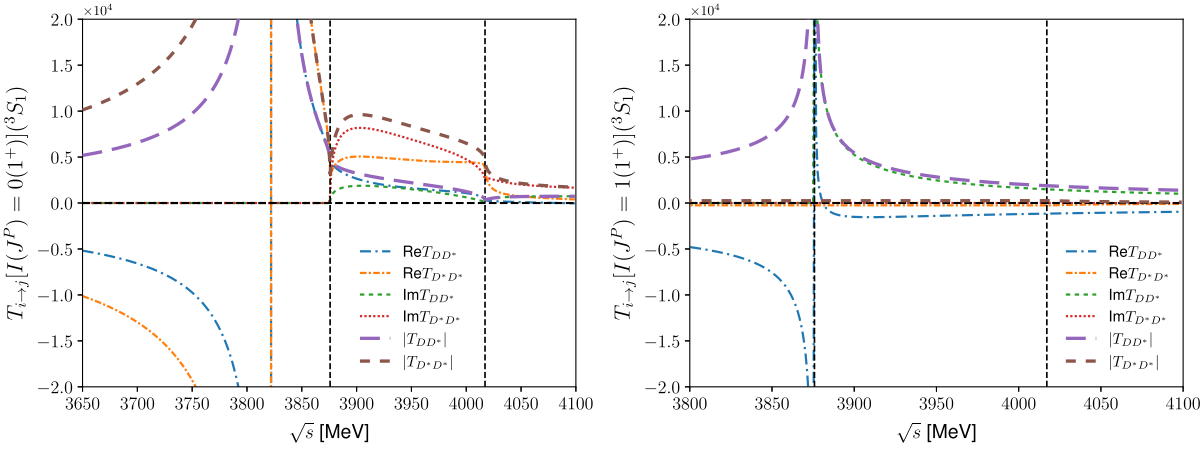


FIG. 10. Transition amplitudes for the elastic DD^* and D^*D^* interactions in the $^3S_1$ channels with isospin $I=0$ (left panel) and $I=1$ (right panel) as functions of the c.m. energy, with all channels switched on. The vertical dashed lines indicate the DD^* and D^*D^* thresholds.

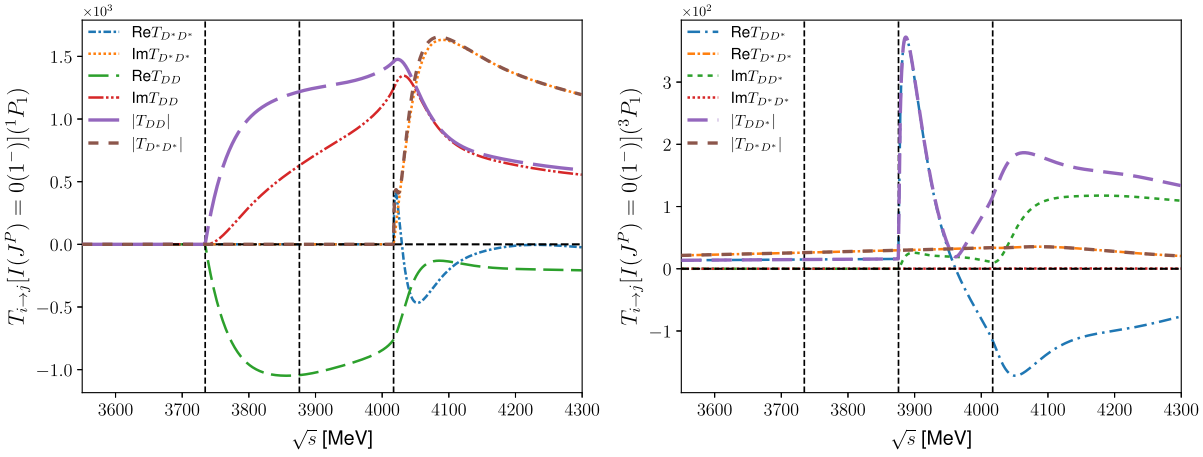


FIG. 11. Transition amplitudes for the elastic DD, DD^*, and D^*D^* interactions in the $^1P_1$ channel (left panel) and $^3P_1$ channel with $I=0$ (right panel) as functions of the c.m. energy, with all channels switched on. The vertical dashed lines indicate the DD, DD^*, and D^*D^* thresholds.

The left and right panels of Fig. 11 display the transition amplitudes for the $^1P_1$ and $^3P_1$ channels with $I=0$, respectively. The results shown in Fig. 11 indicate that the resonance with negative parity consists of both the isoscalar $^1P_1$ and $^3P_1$ channels. Thus, this negative-parity tetraquark state emerges as a P-wave mixed state, meaning that it cannot be identified as a molecular state.

C. Pole positions of the tetraquark states and their coupling strengths

We can examine the pole positions of the tetraquark states by scanning each Riemann sheet of the transition amplitude in the complex energy plane. In the doubly charm sector, three hadronic channels are considered: DD, DD^*, and D^*D^*. Due to the partial-wave decomposition, however, only two channels are effectively coupled, which gives rise to four different Riemann sheets. The distinction between the physical and unphysical sheets is determined by the sign of the imaginary part in Eq. (9), with the physical(unphysical) sheet denoted by $+(-)$. Accordingly, the four sheets can be labeled as $(DD^{(*)}, D^*D^*) = \{(+,+),(+,-),(-,+),(-,-)\}$.

The resulting pole positions and coupling strengths to each channel are listed in Table I. Note that the units of the coupling strengths are given in GeV. They can be extracted from the physical (unphysical) sheet of the transition amplitudes in the vicinity of the pole position $\sqrt{s_R}$ as follows,

$$T_{a\to a}(\sqrt{s}) = 4\pi \frac{g_a^2}{s - s_R}, \tag{29}$$

where the residue g_a (g_b) is the coupling strength corresponding to channel a (b).

As discussed above, we can identify four states with total spin $J=1$: three axial-vector tetraquark states with positive parity and one vector tetraquark with negative parity. In the isoscalar channel, we find a DD^* bound state at 3823.058 MeV on the real axis. Its coupling strength to the D^*D^* channel is the most dominant, followed by that to the DD^* channel. The coupling strengths to all other channels are either negligible or vanish. Thus, inclusion of the D^*D^* channel is essential to form this bound state. The second isoscalar axial-vector tetraquark state appears as a resonance located at $\sqrt{s_R} = (4102.326 - i93.044)$ MeV in the $(+,-)$ sheet. We find that its coupling strengths to the DD^* and D^*D^* channels dominate over all others, similar to the case of $T_{cc}(3823)$. Since it lies above the D^*D^* threshold, it can decay into both the DD^* and D^*D^* channels.

The isovector axial-vector tetraquark state also emerges as a bound state on the real axis at 3875.677 MeV. It lies almost exactly at the DD^* threshold, with a binding energy given by the small value $\delta m = m_{DD^*} - m_R = 0.0328$ MeV, indicating a loosely bound state. This state is in good agreement with the existing $T_{cc}(3875)$ state reported by the LHCb Collaboration [8]. Though the quantum numbers of the $T_{cc}(3875)$ have not been clearly identified, we consider it favorably as an isovector doubly charmed tetraquark state. It is remarkable to observe that its coupling strength to the DD^* channel is the most dominant. This implies that the $T_{cc}(3875)$ can be regarded as a DD^* molecular state.

As discussed previously, an interesting feature of the present work is that we also predict an isoscalar tetraquark resonance with negative parity in addition to the positive-parity ones. It appears in the $(-,-)$ sheet at approximately 5 MeV above the D^*D^* threshold, with a total width of 93.85 MeV. It is noteworthy that the contributions from higher partial waves such as $^5P_1$ and $^5F_1$ are sizable in the coupling strengths to the D^*D^* channel. Thus, by examining the coupling strengths to various channels, we understand that this negative-parity tetraquark state emerges as

TABLE IV. Dependence of the pole positions on the reduced cutoff mass $\Lambda_0 = \Lambda - m_{\rm ex}$.

	Λ_0 (MeV)		
Tetraquark states (J^P)	500	600	700
$T_{cc}^{I=0}(3823)(1^+)$	3867.488	3823.06	3750.0
$T_{cc}^{I=0}(4102)(1^+)$	$4103.260 - i82.05$	$4102.326 - i83.044$	$4102.346 - i84.15$
$T_{cc}^{I=1}(3875)(1^+)$	Cusp	3875.677	3871.78
$T_{cc}^{I=0}(4090)(1^-)$	$4063.66 - i67.47$	$4089.67 - i41.88$	Virtual state

the most dynamically generated one. It may possibly be regarded as a genuine tetraquark state. In Table III, we summarize the results for the pole positions of the T_{cc} resonances, and coupling strengths to the channels involved.

D. Uncertainty of the reduced cutoff mass

Though we do not fit the values of the reduced cutoff mass Λ_0, it is important to estimate the uncertainty arising from variations in Λ_0. We examine the four different tetraquark states produced in the present framework with Λ_0 varied from 500 to 700 MeV. The central value, $\Lambda_0 = 600$ MeV, is adopted in the current work.

Table IV shows how the pole positions change as Λ_0 varies. When we take $\Lambda_0 = 500$ MeV, which is considered to be phenomenologically rather soft, $T_{cc}(3875)$ reduces to a cusp structure. The mass of $T_{cc}(3823)$ increases by about 45 MeV. The $T_{cc}(4102)$ remains almost unchanged. On the other hand, the mass of the negative-parity $T_{cc}(4090)$ is reduced by about 25 MeV, while its width increases. When we use $\Lambda_0 = 700$ MeV, the mass of $T_{cc}(3875)$ remains nearly stable, whereas that of $T_{cc}(3823)$ continues to decrease. The $T_{cc}(4102)$ remains nearly unchanged. Interestingly, the negative-parity $T_{cc}(4090)$ becomes a virtual state. As long as Λ_0 is kept within the range of (600–700) MeV, the most significant tetraquark state $T_{cc}(3875)$ remains almost robust.

IV. SUMMARY AND CONCLUSIONS

In the present work, we have investigated the production mechanism of the doubly charmed tetraquark states within a coupled-channel framework. The kernel amplitudes are constructed by using an effective Lagrangian that respects heavy quark symmetry, chiral symmetry, SU(3) flavor symmetry, and hidden local symmetry. The scattering equation is solved in the Blankenbecler-Sugar scheme, which is a three-dimensional reduction of the Bethe-Salpeter equation. We have examined the pole structures of the resulting transition amplitudes and the corresponding coupling strengths to different channels. The cutoff masses are restricted to a reduced form $\Lambda_0 = \Lambda - m_{\rm ex}$, in order to minimize model dependence.

By analyzing the partial-wave kernel amplitudes, we have shown that the isoscalar–axial-vector- and isovector–axial-vector exhibit strong attractions in the S wave, and give rise to three bound states. On the other hand, the negative-parity resonances appear as P-wave mixed states, which do not qualify as hadronic molecules. We have demonstrated that the isoscalar–axial-vector channel produces a bound state at 3823 MeV and a resonance at $(4102 - i93)$ MeV, while the vector-isovector channel generates a looosely bound state at 3875 MeV. These results support the interpretation of the observed $T_{cc}(3875)^+$ state as a DD^* molecular state in the isovector channel. Moreover, we have predicted a negative-parity isoscalar resonance around 4090 MeV. Finally, we have investigated the dependence of the pole positions on the reduced cutoff mass Λ_0, and found that the main features of the $T_{cc}(3875)$ remain robust within the range $\Lambda_0 = (600–700)$ MeV.

ACKNOWLEDGMENTS

The present work was supported by Inha University (Grant No. 75463-1) in 2025.

DATA AVAILABILITY

The data that support the findings of this article are not publicly available upon publication because it is not technically feasible and/or the cost of preparing, depositing, and hosting the data would be prohibitive within the terms of this research project. The data are available from the authors upon reasonable request.

[1] S. K. Choi *et al.* (Belle Collaboration), Phys. Rev. Lett. **91**, 262001 (2003).
[2] R. F. Lebed, R. E. Mitchell, and E. S. Swanson, Prog. Part. Nucl. Phys. **93**, 143 (2017).
[3] F.-K. Guo, C. Hanhart, U.-G. Meißner, Q. Wang, Q. Zhao, and B.-S. Zou, Rev. Mod. Phys. **90**, 015004 (2018); **94**, 029901(E) (2022).
[4] F.-K. Guo, X.-H. Liu, and S. Sakai, Prog. Part. Nucl. Phys. **112**, 103757 (2020).
[5] Y. Yamaguchi, A. Hosaka, S. Takeuchi, and M. Takizawa, J. Phys. G **47**, 053001 (2020).
[6] H.-X. Chen, W. Chen, X. Liu, Y.-R. Liu, and S.-L. Zhu, Rep. Prog. Phys. **86**, 026201 (2023).
[7] L. Meng, B. Wang, G.-J. Wang, and S.-L. Zhu, Phys. Rep. **1019**, 1 (2023).
[8] R. Aaij *et al.* (LHCb Collaboration), Nat. Phys. **18**, 751 (2022).
[9] R. Aaij *et al.* (LHCb Collaboration), Nat. Commun. **13**, 3351 (2022).
[10] J. l. Ballot and J. M. Richard, Phys. Lett. **123B**, 449 (1983).
[11] S. Zouzou, B. Silvestre-Brac, C. Gignoux, and J. M. Richard, Z. Phys. C **30**, 457 (1986).
[12] H.-C. Kim and M. Shmatikov, Phys. Lett. B **375**, 310 (1996).
[13] S. Pepin, F. Stancu, M. Genovese, and J. M. Richard, Phys. Lett. B **393**, 119 (1997).
[14] M. A. Moinester, Z. Phys. A **355**, 349 (1996).
[15] D. Ebert, R. N. Faustov, V. O. Galkin, and W. Lucha, Phys. Rev. D **76**, 114015 (2007).
[16] F. S. Navarra, M. Nielsen, and S. H. Lee, Phys. Lett. B **649**, 166 (2007).
[17] S. Ohkoda, Y. Yamaguchi, S. Yasui, K. Sudoh, and A. Hosaka, Phys. Rev. D **86**, 034019 (2012).
[18] E. J. Eichten and C. Quigg, Phys. Rev. Lett. **119**, 202002 (2017).
[19] S.-Q. Luo, K. Chen, X. Liu, Y.-R. Liu, and S.-L. Zhu, Eur. Phys. J. C **77**, 709 (2017).
[20] R. Zhu, X. Liu, H. Huang, and C.-F. Qiao, Phys. Lett. B **797**, 134869 (2019).
[21] L. Tang, B.-D. Wan, K. Maltman, and C.-F. Qiao, Phys. Rev. D **101**, 094032 (2020).
[22] Y. Tan, W. Lu, and J. Ping, Eur. Phys. J. Plus **135**, 716 (2020).
[23] J.-B. Cheng, S.-Y. Li, Y.-R. Liu, Z.-G. Si, and T. Yao, Chin. Phys. C **45**, 043102 (2021).
[24] M. Praszalowicz, Phys. Rev. D **106**, 114005 (2022).
[25] J. Zhang, J.-B. Wang, G. Li, C.-S. An, C.-R. Deng, and J.-J. Xie, Eur. Phys. J. C **82**, 1126 (2022).
[26] M. Kucab and M. Praszalowicz, Phys. Rev. D **109**, 076005 (2024).
[27] M. N. Anwar and T. J. Burns, Phys. Lett. B **847**, 138248 (2023).
[28] Q. Meng, E. Hiyama, M. Oka, A. Hosaka, and C. Xu, Phys. Lett. B **846**, 138221 (2023).
[29] W.-C. Dong and Z.-G. Wang, Nucl. Phys. **B1012**, 116828 (2025).
[30] H. Ren, F. Wu, and R. Zhu, Adv. High Energy Phys. **2022**, 9103031 (2022).
[31] M. Albaladejo, Phys. Lett. B **829**, 137052 (2022).
[32] L.-Y. Dai, X. Sun, X.-W. Kang, A. P. Szczepaniak, and J.-S. Yu, Phys. Rev. D **105**, L051507 (2022).
[33] M.-L. Du, V. Baru, X.-K. Dong, A. Filin, F.-K. Guo, C. Hanhart, A. Nefediev, J. Nieves, and Q. Wang, Phys. Rev. D **105**, 014024 (2022).
[34] X.-Z. Ling, M.-Z. Liu, L.-S. Geng, E. Wang, and J.-J. Xie, Phys. Lett. B **826**, 136897 (2022).
[35] K. Chen, R. Chen, L. Meng, B. Wang, and S.-L. Zhu, Eur. Phys. J. C **82**, 581 (2022).
[36] A. Feijoo, W. H. Liang, and E. Oset, Phys. Rev. D **104**, 114015 (2021).
[37] S. Fleming, R. Hodges, and T. Mehen, Phys. Rev. D **104**, 116010 (2021).
[38] H.-W. Ke, X.-H. Liu, and X.-Q. Li, Eur. Phys. J. C **82**, 144 (2022).
[39] Q. Xin and Z.-G. Wang, Eur. Phys. J. A **58**, 110 (2022).
[40] M.-J. Zhao, Z.-Y. Wang, C. Wang, and X.-H. Guo, Phys. Rev. D **105**, 096016 (2022).
[41] S. S. Agaev, K. Azizi, and H. Sundu, J. High Energy Phys. 06 (2022) 057.
[42] Y. Kamiya, T. Hyodo, and A. Ohnishi, Eur. Phys. J. A **58**, 131 (2022).
[43] T. Asanuma, Y. Yamaguchi, and M. Harada, Phys. Rev. D **110**, 074030 (2024).
[44] I. Vidana, A. Feijoo, M. Albaladejo, J. Nieves, and E. Oset, Phys. Lett. B **846**, 138201 (2023).
[45] M. Abolnikov, V. Baru, E. Epelbaum, A. A. Filin, C. Hanhart, and L. Meng, Phys. Lett. B **860**, 139188 (2025).
[46] L. Meng, E. Ortiz-Pacheco, V. Baru, E. Epelbaum, M. Padmanath, and S. Prelovsek, Phys. Rev. D **111**, 034509 (2025).
[47] T. Whyte, D. J. Wilson, and C. E. Thomas (Hadron Spectrum Collaboration), Phys. Rev. D **111**, 034511 (2025).
[48] W.-L. Wu, Y. Ma, Y.-K. Chen, L. Meng, and S.-L. Zhu, Phys. Rev. D **110**, 094041 (2024).
[49] J.-L. Lu, M. Song, P. Wang, J.-Y. Guo, G. Li, and X. Luo, Eur. Phys. J. C **85**, 920 (2025).
[50] M. Padmanath and S. Prelovsek, Phys. Rev. Lett. **129**, 032002 (2022).
[51] Y. Lyu, S. Aoki, T. Doi, T. Hatsuda, Y. Ikeda, and J. Meng, Phys. Rev. Lett. **131**, 161901 (2023).
[52] M. Mai, U.-G. Meißner, and C. Urbach, Phys. Rep. **1001**, 1 (2023).
[53] M. Döring, J. Haidenbauer, M. Mai, and T. Sato, arXiv: 2505.02745.
[54] R. Machleidt, K. Holinde, and C. Elster, Phys. Rep. **149**, 1 (1987).
[55] J. Haidenbauer and U.-G. Meissner, Phys. Rev. C **72**, 044005 (2005).
[56] D. Lohse, J. W. Durso, K. Holinde, and J. Speth, Nucl. Phys. **A516**, 513 (1990).
[57] G. Janssen, J. W. Durso, K. Holinde, B. C. Pearce, and J. Speth, Phys. Rev. Lett. **71**, 1978 (1993).
[58] G. Janssen, B. C. Pearce, K. Holinde, and J. Speth, Phys. Rev. D **52**, 2690 (1995).
[59] C. Schutz, J. Haidenbauer, J. Speth, and J. W. Durso, Phys. Rev. C **57**, 1464 (1998).
[60] H.-C. Kim, J. W. Durso, and K. Holinde, Phys. Rev. C **49**, 2355 (1994).

[61] G. Janssen, K. Holinde, and J. Speth, Phys. Rev. C **54**, 2218 (1996).
[62] A. Reuber, K. Holinde, H.-C. Kim, and J. Speth, Nucl. Phys. **A608**, 243 (1996).
[63] R. Blankenbecler and R. Sugar, Phys. Rev. **142**, 1051 (1966).
[64] R. Aaron, R. D. Amado, and J. E. Young, Phys. Rev. **174**, 2022 (1968).
[65] S. Clymton and H.-C. Kim, Phys. Rev. D **106**, 114015 (2022).
[66] S. Clymton and H.-C. Kim, Phys. Rev. D **108**, 074021 (2023).
[67] S. Clymton and H.-C. Kim, Phys. Rev. D **110**, 114002 (2024).
[68] H.-J. Kim and H.-C. Kim, Prog. Theor. Exp. Phys. **2024**, 073D01 (2024).
[69] R. Aaij *et al.* (LHCb Collaboration), Phys. Rev. Lett. **115**, 072001 (2015).
[70] R. Aaij *et al.* (LHCb Collaboration), Phys. Rev. Lett. **122**, 222001 (2019).
[71] R. Aaij *et al.* (LHCb Collaboration), Phys. Rev. Lett. **128**, 062001 (2022).
[72] S. Clymton, H.-C. Kim, and T. Mart, Phys. Rev. D **110**, 094014 (2024).
[73] A. Ali *et al.* (GlueX Collaboration), Phys. Rev. Lett. **123**, 072001 (2019).
[74] S. Adhikari *et al.* (GlueX Collaboration), Phys. Rev. C **108**, 025201 (2023).
[75] R. Aaij *et al.* (LHCb Collaboration), Sci. Bull. **66**, 1278 (2021).
[76] R. Aaij *et al.* (LHCb Collaboration), Phys. Rev. Lett. **131**, 031901 (2023).
[77] I. Adachi *et al.* (Belle and Belle II Collaborations), arXiv:2502.09951.
[78] S. Clymton, H.-C. Kim, and T. Mart, Phys. Rev. D **112**, 014041 (2025).
[79] S. Clymton, H.-C. Kim, and T. Mart, Phys. Rev. D **112**, 034015 (2025).
[80] S. R. Coleman, J. Wess, and B. Zumino, Phys. Rev. **177**, 2239 (1969).
[81] C. G. Callan, Jr., S. R. Coleman, J. Wess, and B. Zumino, Phys. Rev. **177**, 2247 (1969).
[82] M. Bando, T. Kugo, S. Uehara, K. Yamawaki, and T. Yanagida, Phys. Rev. Lett. **54**, 1215 (1985).
[83] M. Bando, T. Kugo, and K. Yamawaki, Nucl. Phys. **B259**, 493 (1985).
[84] S. Ahmed *et al.* (CLEO Collaboration), Phys. Rev. Lett. **87**, 251801 (2001).
[85] R. Casalbuoni, A. Deandrea, N. Di Bartolomeo, R. Gatto, F. Feruglio, and G. Nardulli, Phys. Rep. **281**, 145 (1997).
[86] C. Isola, M. Ladisa, G. Nardulli, and P. Santorelli, Phys. Rev. D **68**, 114001 (2003).
[87] S. Navas *et al.* (Particle Data Group), Phys. Rev. D **110**, 030001 (2024).
[88] H.-J. Kim and H.-C. Kim, Phys. Rev. D **102**, 014026 (2020).
[89] K. Kawarabayashi and M. Suzuki, Phys. Rev. Lett. **16**, 255 (1966).
[90] Riazuddin and Fayyazuddin, Phys. Rev. **147**, 1071 (1966).
[91] J.-Y. Kim and H.-C. Kim, Phys. Rev. D **97**, 114009 (2018).
[92] J.-Y. Kim, H.-C. Kim, G.-S. Yang, and M. Oka, Phys. Rev. D **103**, 074025 (2021).
[93] H.-Y. Won, J.-Y. Kim, and H.-C. Kim, Phys. Rev. D **106**, 114009 (2022).